Asymmetric Structural Features in Single Supported Lipid Bilayers Containing Cholesterol and G_{M1} Resolved with Synchrotron X-Ray Reflectivity

Christian Reich,* Margaret R. Horton,† Bärbel Krause,‡ Alice P. Gast,§ Joachim O. Rädler,* and Bert Nickel*
*Department für Physik, Ludwig-Maximilians-Universität, Munich, Germany; †Department of Chemical Engineering, Massachusetts Institute of Technology, Cambridge, Massachusetts; ‡European Synchrotron Radiation Facility, Grenoble, France; and §Department of Chemical Engineering, Lehigh University, Bethlehem, Pennsylvania

ABSTRACT The cell membrane comprises numerous protein and lipid molecules capable of asymmetric organization between leaflets and liquid-liquid phase separation. We use single supported lipid bilayers (SLBs) to model cell membranes, and study how cholesterol and asymmetrically oriented ganglioside receptor G_{M1} affect membrane structure using synchrotron x-ray reflectivity. Using mixtures of cholesterol, sphingomyelin, and 1,2-dioleoyl-*sn*-glycero-3-phosphocholine, we characterize the structure of liquid-ordered and liquid-disordered SLBs in terms of acyl-chain density, headgroup size, and leaflet thickness. SLBs modeling the liquid-ordered phase are 10 Å thicker and have a higher acyl-chain electron density ($\langle\rho_{chain}\rangle = 0.33\ e^-/Å^3$) compared to SLBs modeling the liquid-disordered phase, or pure phosphatidylcholine SLBs ($\langle\rho_{chain}\rangle = 0.28\ e^-/Å^3$). Incorporating G_{M1} into the distal bilayer leaflet results in membrane asymmetry and thickening of the leaflet of 4–9 Å. The structural effect of G_{M1} is more complex in SLBs of cholesterol/sphingomyelin/1,2-dioleoyl-*sn*-glycero-3-phosphocholine, where the distal chains show a high electron density ($\langle\rho_{chain}\rangle = 0.33\ e^-/Å^3$) and the lipid diffusion constant is reduced by ~50%, as measured by fluorescence microscopy. These results give quantitative information about the leaflet asymmetry and electron density changes induced by receptor molecules that penetrate a single lipid bilayer.

INTRODUCTION

Cell membranes are highly heterogeneous structures with numerous lipid and protein species. This heterogeneity is reflected in asymmetric lipid compositions in the inner and outer leaflets of the plasma membrane. Within mammalian membrane leaflets, the degree of saturation and the length of the lipid acyl chains vary among molecules and can locally affect the membrane thickness and induce lateral heterogeneity (1). The major constituents of the outer membrane leaflet of mammalian cells (phospholipids, sphingomyelin, and cholesterol) are capable of phase separation due to attractive interactions between cholesterol and sphingomyelin (2–4). Cholesterol preferentially localizes to the vicinity of sphingomyelin due to hydrogen-bonding between the hydroxyl group of the sphingosine backbone and the polar moiety of the sterol (5,6). The relatively rigid structure of cholesterol and its ability to fit into the interstitial space between the saturated acyl chains of sphingomyelin tighten lipid packing and result in a cholesterol-enriched liquid-ordered phase (L_o) (6), in coexistence with a cholesterol-depleted liquid-disordered phase (L_d) containing mainly unsaturated phospholipids. L_o domains, commonly referred to as lipid rafts (2), are thought to play a role in membrane organization by concentrating different receptor molecules into certain lipid environments (7).

The monosialoganglioside G_{M1} is the receptor for cholera toxin entering the cell through the endocytic pathway and has been shown to localize to raft domains in the outer membrane leaflet (8). The asymmetric localization of receptors within L_o or L_d phases is governed by intermolecular interactions within the membrane. For most natural gangliosides (human, bovine), the high level of saturation of the ceramide moiety may determine the preference of G_{M1} to partition into the L_o phase, although specific interactions of its large oligosaccharide headgroup with nearby sphingomyelin and phosphocholine headgroups may also play a role (7). The leaflet asymmetry of G_{M1} may also induce an asymmetric distribution of cholesterol, whose exact transbilayer distribution is not known (6).

The complex structure of cell membranes often inhibits discrete experimental studies of lipid-lipid interactions. Successful efforts to systematically study intermolecular interactions have been made using simplified biomimetic membranes, which can be engineered with multiple components and lipid asymmetry among the leaflets, mimicking the structure and function of cell membranes. A special class of biomimetic membranes are solid supported lipid bilayers (SLBs), which have proven particularly useful for the application of surface sensitive techniques, such as atomic force microscopy (AFM) (9), x-ray and neutron diffraction (10–13), and methods based on fluorescence microscopy (14,15).

Measuring the height profiles of SLBs with AFM has provided information about lipid bilayer structure and the dimensions of G_{M1} in the membrane. AFM experiments indicate that L_o domains are condensed and have a lipid packing distinct from L_d domains; a relative increase in the

Submitted May 18, 2007, and accepted for publication March 10, 2008.

Address reprint requests to Christian Reich. E-mail: creich@alumni.tum.de.

Bärbel Krause's present address is Institut für Synchrotronstrahlung (ISS), Forschungszentrum Karlsruhe, Germany.

Editor: Thomas J. McIntosh.

0006-3495/08/07/657/12 $2.00

doi: 10.1529/biophysj.107.113068

height of the L_o phase of 8 Å with respect to the surrounding L_d phase has been reported (16). In SLBs containing model L_d/L_d domains and in addition symmetrically distributed G_{M1}, a height difference of 20 Å between G_{M1}-enriched L_o-domains and the surrounding bilayer has been found (17). These AFM studies, however, do not permit conclusions about the absolute thicknesses and densities of the SLBs, and the effect of GM1 on the internal structure of lipid membranes remains unclear.

A method of determining whether membrane receptors prefer condensed lipid environments is to use fluorescence microscopy to assess the partitioning behavior of their labeled conjugates into microscopic L_o/L_d phases (14,18,19) or through detection of changes in the emission spectra of the dye depending on its localization in either the L_o or L_d phase (15,20). In such experiments, however, it is not easily possible to distinguish whether the fluorescence intensity of the labeled conjugate was emitted from the inner or outer membrane leaflet.

Another common technique to indirectly study the structural properties of lipid bilayers is to assess the lateral motion of the dye molecules in a SLB using fluorescence recovery after photobleaching (FRAP) (21), continuous bleaching (22), or fluorescence correlation spectroscopy (FCS) (16). With these measurements, lipid diffusion in the bilayer is quantified, providing information about the fluidity of the lipids. Recent FCS studies in model lipid raft SLBs on mica show that lipid diffusion is more than tenfold slower in L_o domains compared to L_d domains (16), suggesting that lipid rafts are condensed entities (3). Membrane receptors have also been shown to influence lipid mobility: FRAP studies on SLBs with G_{M1} symmetrically distributed among the leaflets demonstrate that G_{M1} decreases the mobility of surrounding lipids (23), particularly if the surrounding lipids are near a gel phase transition (24). Possible mechanisms of lipid fluidity moderation by G_{M1} are lateral condensation of lipid molecules (25) or local lipid immobilization due to a disruption of lipid headgroup packing, as reported for lipid monolayer systems (26). To characterize the packing of cholesterol and receptor molecules in the bilayer, and to assess leaflet asymmetry, molecular-level structural methods on single lipid bilayers are necessary.

Such a direct method to examine lipid bilayer structure is x-ray surface diffraction; in principle, the high sensitivity of x rays to the electron density distribution within SLBs should allow the electron densities and thicknesses of the individual lipid bilayer leaflets to be determined. X-ray reflectivity at solid-liquid interfaces has been used to study the structure of SLBs with subnanometer resolution (10,12,27) and there has been progress toward understanding heterogeneous lipid mixtures using this technique (11). The structural differences between gel and fluid lipid bilayers have been characterized in terms of electron density and leaflet thickness. However, an important question remains how L_o bilayers containing cholesterol are structurally distinct from fluid L_d bilayers.

In this work, we directly measure how ovine G_{M1} impacts the structure of model lipid bilayers. We characterize single SLBs at the solid-liquid interface with x-ray reflectivity using a microfluidic sample chamber described in previous work (12,27,28). First, a one-component SLB in the fluid phase is characterized and lipid packing modifications after asymmetric insertion of G_{M1} are analyzed. We also identify the structural characteristics of SLBs representing either condensed L_o or fluid L_d bilayers; for this, we estimate the lipid compositions based on the corresponding pure L_o and pure L_d phases in the phase diagram of giant unilamellar vesicles of ternary mixtures of cholesterol, sphingomyelin, and 1,2-dioleoyl-*sn*-glycero-3-phosphocholine (DOPC) (29,30). Finally, a series of SLBs from ternary lipid mixtures capable of L_o/L_d phase separation are investigated and the structural modifications of these SLBs upon asymmetric G_{M1} insertion are analyzed in terms of acyl-chain density and leaflet thickness. These structural x-ray studies are complemented by fluorescence microscopy and continuous bleaching on the same samples. We investigate lipid dynamics by measuring lipid diffusion before and after incorporation of G_{M1} into the bilayers.

MATERIALS AND METHODS

Chemicals

The lipids 1-stearoyl-2-oleoyl-*sn*-glycero-3-phosphocholine (SOPC), 1,2-dioleoyl-*sn*-glycero-3-phosphocholine (DOPC), brain sphingomyelin (bSM), cholesterol, and the ovine brain ganglioside G_{M1} are purchased from Avanti Polar Lipids (Alabaster, AL). Cholera toxin subunit B, labeled with Alexa Fluor 488 (Alexa488-CTB), and Texas Red labeled 1,2-dihexadecanoyl-*sn*-glycero-3-phosphoethanolamine, triethylammonium salt (TR-DPPE) are purchased from Invitrogen (Karlsruhe, Germany). HPLC-grade chloroform, acetone, isopropanol, and ethanol are obtained from Carl Roth (Karlsruhe, Germany). Reagent-grade NH_4OH, HCl (37%), and H_2O_2 are purchased from Sigma (St. Louis, MO). NaCl, $CaCl_2$, $MgCl_2$, phosphate-buffered saline, and HEPES are also from Sigma. Buffer I is composed of 10 mM HEPES, 100 mM NaCl, 2 mM $CaCl_2$, 2 mM $MgCl_2$ at pH = 7.4 and buffer II is composed of 138 mM NaCl, 2.7 mM KCl, 10 mM Na_2HPO_4, 2 mM KH_2PO_4 at pH = 7.4 (0.01 M phosphate-buffered saline). Buffers are prepared in deionized (DI) water from Millipore (Billerica, MA).

Substrate treatment

Polished 6″ silicon wafers with a 100-nm thermal oxide layer are cut into small pieces of size 20 × 15 mm^2 (Crystec, Berlin, Germany). The average surface roughness of the polished wafers is 3 Å, as indicated by the manufacturer and verified in our lab using x-ray reflectivity. Before experiments, the substrates are cleaned by sonication in isopropanol for 10 min followed by rinsing with DI water. Afterwards, a three-stage chemical cleaning treatment is applied: first, the substrates are boiled in acetone for 10 min, then in 1:1:5 H_2O_2/HCl/H_2O by volume for 15 min at 150°C, then in 1:1:5 H_2O_2/NH_4OH/H_2O for another 15 min at 150°C. After each step, the substrates are rinsed thoroughly with DI water. The substrates are stored in DI water until further use.

Sample chamber assembly

Plastic sample chambers (μ-Slide I) are purchased from Ibidi (München, Germany) and are modified to embed the silicon wafer pieces (27). The clean

SiO_2 substrates are affixed to the base of the chamber. The substrates are dried with a nitrogen stream and immediately glued into the chambers using two-component epoxy glue that hardens in 5 min (UHU, Bühl, Germany). After allowing the epoxy glue to dry for 30 min, the chambers with glued-in substrates are placed under vacuum for 6 h for final hardening. The microfluidic channel inside the sample chamber is then filled with buffer I.

Preparation of large unilamellar vesicles

All lipid mixtures are prepared in HPLC-grade chloroform in clean glass vials, except for TR-DPPE, which is prepared in a 1:1 mixture by volume of chloroform and methanol. The chloroform is first evaporated from each vial in a nitrogen stream followed by 8 h evacuation in a vacuum chamber to completely remove the solvent. The dry lipid film in the vials is suspended in buffer I at a final concentration of 1 mg/mL and heated to 50°C for 1 h. The extrusion method (31) is used to prepare large unilamellar vesicles (LUVs) for experiments. The lipid suspension is vortexed and then passed 11 times through a polycarbonate filter with uniform 100 nm pores (Avanti Polar Lipids). For compositions of cholesterol/DOPC/bSM, lipids are extruded at a temperature above the lipid phase transition temperature, T_m, using the lipid phase diagram of giant unilamellar vesicles (GUVs) for these lipid compositions as a reference to determine T_m (32).

Vesicle fusion via osmotic rupture

The LUVs are used to form SLBs on the freshly prepared substrates in the sample chambers via vesicle fusion (33): the LUVs are injected into chambers prewetted with buffer I and incubated for 3 h, allowing the LUVs to adhere on the substrate. The temperature of the LUVs is kept above T_m during incubation. The chamber is then flushed with DI water at room temperature to assist the rupture of the LUVs due to osmotic stress, forming a continuous lipid bilayer on the substrate. The surface area coverage is complete as verified by fluorescence microscopy. After formation of the continuous supported bilayer, the samples are kept above T_m for another 4 h and then slowly cooled down to room temperature. The samples are flushed several times with buffer II before the measurements to remove unruptured vesicles.

G_{M1} incorporation into SLBs

Buffer II is added to G_{M1} in powder form at a concentration of 1 mg/mL and the solution is stored at 4°C. G_{M1} in such aqueous solutions can aggregate and form micelles (34) and this G_{M1} concentration of 640 μM is well above the critical micelle concentration of 3.32 μM (35). Sample chambers with SLB-coated substrates are rinsed with buffer II, then filled with 100 μL of the G_{M1} solution and left to incubate for 4 h. G_{M1} can spontaneously partition into the outer leaflet of lipid bilayers up to concentrations of 30% (36) due to its amphiphilic character (37,38) and cone-shaped structure (39).

X-ray reflectivity measurements

The samples are prepared and measured at the undulator beamline ID01 at the European Synchrotron Radiation Facility in Grenoble, France. For x-ray reflectivity, the sample chamber and beamline setup previously described (27) is used. A schematic is shown in Fig. 1. The x-ray energy is 19.5 keV ($\lambda = 0.623$ Å) and sample chambers are mounted in horizontal scattering geometry. The incidental beam cross section is 20×200 μm^2 (vertical $\times$ horizontal). A small vertical post-sample aperture suppresses reflectivity from the thin top foil of the sample chamber. Air scattering is minimized by evacuated beam guides with Kapton windows positioned close to the sample chamber. The intensity is collected with a NaI detector. All reflectivity data are measured at room temperature and for each sample at least three different spots on the sample are recorded. Each spot is first characterized before reflectivity by fluorescence microscopy to verify complete surface coverage, removal of all unruptured vesicles, and homogeneity across the cross section area of the x-ray beam. Repeated reflectivity measurements on previously illuminated spots are avoided. In most cases, no variation is observed among the different spots. The oxide layer on top of the silicon substrate can give an additional contribution to the scattering contrast in the reflectivity, in particular for high resolution measurements with many data points. This contribution is suppressed by choosing a well-defined step width for the recorded data points (see Supplementary Material, Data S1). The presented reflectivity data are corrected for background, sample illumination (footprint), and normalized to the Fresnel reflectivity (R/R_F), where

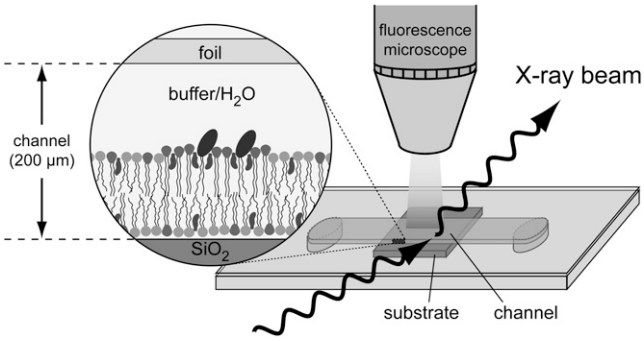

FIGURE 1 Schematic of the microfluidic sample chamber used for x-ray and fluorescence microscopy experiments.

$$R_F = \left| \frac{1 - \sqrt{1 - (q_c/q_z)^2}}{1 + \sqrt{1 - (q_c/q_z)^2}} \right|^2 . \quad (1)$$

The momentum transfer normal to the interface is denoted as q_z and the momentum transfer at the critical angle of total reflection is q_c. It should be noted that x-ray reflectivity laterally averages the electron density within the illuminated surface area. Thus these measurements do not distinguish between discrete and laterally segregated microscopic phases. In our experimental configuration, the x-ray beam impinges on the surface with typical grazing angles between 0.02° and 1.5° and therefore illuminates large surface areas. In the vicinity of the first characteristic minima of most of our reflectivity data, the typical illuminated surface area of 2 mm $\times$ 0.2 mm corresponds to an incidence angle of 0.57°. At small angles ($q_z < 0.1$ Å^{-1}), the illuminated area exceeds the effective sample surface and the reflectivity signal can contain contributions from the glue/silicon interface at the sample edges (see Data S1).

X-ray data evaluation

Starting models

Before data analysis, we calculated model density profiles for all samples, based on previously reported and/or calculated electron densities and thicknesses for the lipid components (10,11,40–44). The headgroups of the lipids in this study consist of a glycerol or sphingosine backbone and a phosphate group with a choline moiety. This chemical structure is modeled with two slabs to account for a possible asymmetry in the electron density distribution of the headgroups. The hydrophobic core of a lipid bilayer is modeled using two slabs for the opposing lipid chains and a slab for the region where the chains meet. Additional slabs are introduced to account for the presence of extended headgroups, as is the case in measurements with G_{M1}. The calculated slabs are used as the initial model to fit the reflectivity data using the dynamical theory of Parratt (45).

Data fitting

Starting from the calculated slab models, the data are fit using least-squares optimization. The electron densities and thicknesses of the slabs are varied independently for χ^2 minimization, with an interface roughness of 3 Å. This value accounts for the roughness of the substrate. The roughness of a well-defined, supported lipid bilayer is expected to correlate to this interface roughness due to the strong physisorption to the substrate. Upper and lower boundaries for the electron densities are 0.2 and 0.34 $e^-/Å^3$ for the lipid acyl chains, and 0.3 and 0.55 $e^-/Å^3$ for the headgroup regions, based on literature values. The χ^2-minimization is done by taking advantage of the full momentum transfer range of the data. This allows us to fit the data without imposing further constraints on the model.

Precision of electron density distributions

To judge the accuracy of our modeling, we estimate the intrinsic spatial resolution as $\pi/q_{max} \sim 6$ Å, based on the dynamic range of our reflectivity data which extends up to $q_{max} = 0.5–0.6$ Å^{-1} (46). Each slab is defined by its electron density ρ, thickness d, and roughness σ. These parameters are correlated, and for the n^{th} slab in a model profile, the specific values ρ_n, d_n, and σ_n carry direct physical information only if $\sigma_n \ll d_n$ (47,48). In this case, the slab can be related to a distinct region in the lipid bilayer. Its electron density distribution $\tilde{\rho}_n(z)$ is then represented by two error functions, which smear the corresponding slab ρ_n at both interfaces (z_n, $z_n + d_n$) with a Gaussian roughness σ,

$$\tilde{\rho}_n(z) = \frac{\rho_n}{2}\left[1 + \mathrm{erf}\left(\frac{z - z_n}{\sqrt{2}\sigma}\right)\right] \times \frac{\rho_n}{2}\left[1 - \mathrm{erf}\left(\frac{z - (z_n + d_n)}{\sqrt{2}\sigma}\right)\right]. \quad (2)$$

The distance from the substrate along the bilayer normal is denoted as z. Here, the roughness is uniform, $\sigma_n = \sigma = 3$ Å. For $\sigma \ll d_n$, the number of electrons per volume is conserved after smearing the slab. This is verified by integrating $\tilde{\rho}_n(z)$ along z and by comparing the result with $\rho_n \cdot d_n$. In this study, we consider a maximum relative error

$$\varepsilon = \left|1 - \int \tilde{\rho}_n(z)\,dz/(\rho_n d_n)\right| \le 10^{-3}, \quad (3)$$

as the limiting value for each $\tilde{\rho}_n(z)$-distribution. For all samples in this study, the slabs representing the lipid acyl-chain regions match the criteria established by Eq. 3. For slabs with $\sigma \ll d_n$, the error becomes $\varepsilon \gg 10^{-3}$ and Eq. 2 cannot be applied to model the electron density distribution. For most samples in this study, this is the case for the lipid headgroup slabs. While slabs with $\sigma \ll d_n$ cannot be interpreted physically, the smeared overall profile is still a physically valid display of the lipid bilayer, and structural details can be extracted as subsequently described.

Extracting bilayer parameters

We proceed as follows: first, the slabs representing the acyl chains, fulfilling Eq. 3, are smeared according to Eq. 2. The procedure is exemplified in Fig. 3, where the electron density distributions of the acyl chains, $\tilde{\rho}_{chain}(z)$ (without the region between the leaflets), are depicted as green curves. The smeared contributions of the acyl chains ($\tilde{\rho}_{chain}(z)$), and the water and silicon oxide ($\tilde{\rho}_{water}(z), \tilde{\rho}_{Si}(z)$) (*black curves*), are then subtracted from the smeared overall electron density profile. We assign the remaining electron density distribution to the lipid headgroups, $\tilde{\rho}_{head}(z)$, and the region where the acyl chains meet, $\tilde{\rho}_{center}(z)$ (*blue curves* in Fig. 3 *b*). The characteristic width of a headgroup region, b_{head}, is derived from the full width at half-maximum of its $\tilde{\rho}_{head}(z)$-distribution (Fig. 3 *a*). Then, average electron densities for each region are determined by

$$\langle\rho_{head}\rangle = \frac{1}{b_{head}}\int \tilde{\rho}_{head}(z)\,dz. \quad (4)$$

The physical width of the acyl chains, including the terminal acyl groups in the center of the bilayer, is calculated separately for each leaflet as

$$b_{chain} = d_{chain} + \frac{b_{center}}{2}, \quad (5)$$

where d_{chain} is the thickness of the smeared chain slab and b_{center} is the full width at half-maximum of the region where the acyl chains meet. The average electron density for the separate acyl chains is determined by

$$\langle\rho_{chain}\rangle = \frac{1}{b_{chain}}\left[\int \tilde{\rho}_{chain}(z)\,dz + \frac{1}{2}\int \tilde{\rho}_{center}(z)\,dz\right]. \quad (6)$$

Using this decomposition, the parameters $\langle\rho_{head}\rangle$, b_{head}, $\langle\rho_{chain}\rangle$, and b_{chain} for both the proximal and distal leaflets of the membrane are determined.

Fluorescence microscopy

Fluorescence microscopy is performed on-site at the European Synchrotron Radiation Facility using a transportable Axiotech Vario microscope from Carl Zeiss (Oberkochen, Germany), equipped with 10× (NA 0.3) and long distance 63× (NA 0.75) Plan-Neofluar objectives. The uniform oxide layer (100 nm) on the silicon substrate inhibits fluorescence quenching of dye molecules and allows for fluorescence microscopy measurements (49). Images are captured with an ORCA C4742-95 12NR charge-coupled device camera and WASABI imaging software from Hamamatsu Photonics (Tutzing, Germany). Lateral diffusion coefficients of the supported lipid bilayers are determined using continuous bleaching (22); the experimental technique and the procedure for data evaluation is described elsewhere in detail (12,28). For these experiments, a mercury lamp is aligned to ensure homogeneous illumination of the sample. Continuous bleaching data are analyzed using MATLAB software from The MathWorks (Natick, MA).

RESULTS AND DISCUSSION

Structural impact of G_{M1} insertion into single component SLBs

The simplest model for the cell membrane is a single lipid bilayer of only one lipid component. A fluid lipid bilayer of 1-stearoyl-2-oleoyl-*sn*-glycero-3-phosphocholine (SOPC, melting temperature 6°C) provides a well-defined interface for characterizing the structural influence of G_{M1}. The acyl chains of synthetic SOPC (18:0–18:1, 100%) are structurally similar to the ceramide distribution of natural ovine G_{M1} (Avanti Polar Lipids) (acyl-chain abundance: 18:0–18:1, 70%; 20:1–18:0, 25%; and 18:1–20:0, 5%). Thus, the insertion of ovine G_{M1} into an SOPC bilayer should not introduce additional saturated moieties the membrane. Fig. 2 *a* shows the reflectivity of a lipid bilayer of 99.5 mol % SOPC and 0.5 mol % of the fluorescent probe TR-DPPE; the data curve is characteristic for a single lipid bilayer above a solid support (10,27). After incubation for 4 h with excess G_{M1}, we again measure the reflectivity and small but significant changes in the reflectivity are apparent as seen in the normalized scan presented in Fig. 2 *b*. The downward shift in the positions of the minima, from $q_z \sim 0.2$ to 0.18 Å^{-1} and from 0.34 to 0.3 Å^{-1}, qualitatively indicates a thickening of the bilayer.

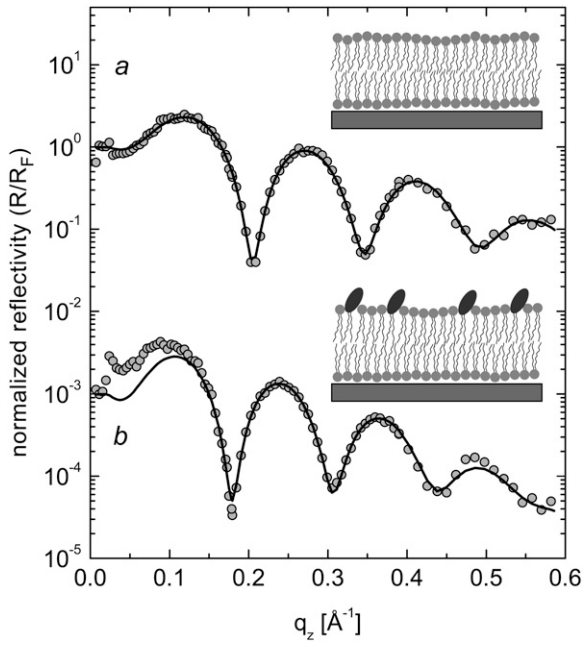

FIGURE 2 Normalized reflectivity scans with fits (*solid lines*) for SOPC before (*a*) and after (*b*) incubation with excess G_{M1}. Sketches illustrate the bilayer structure and asymmetric incorporation of G_{M1} into the distal leaflet.

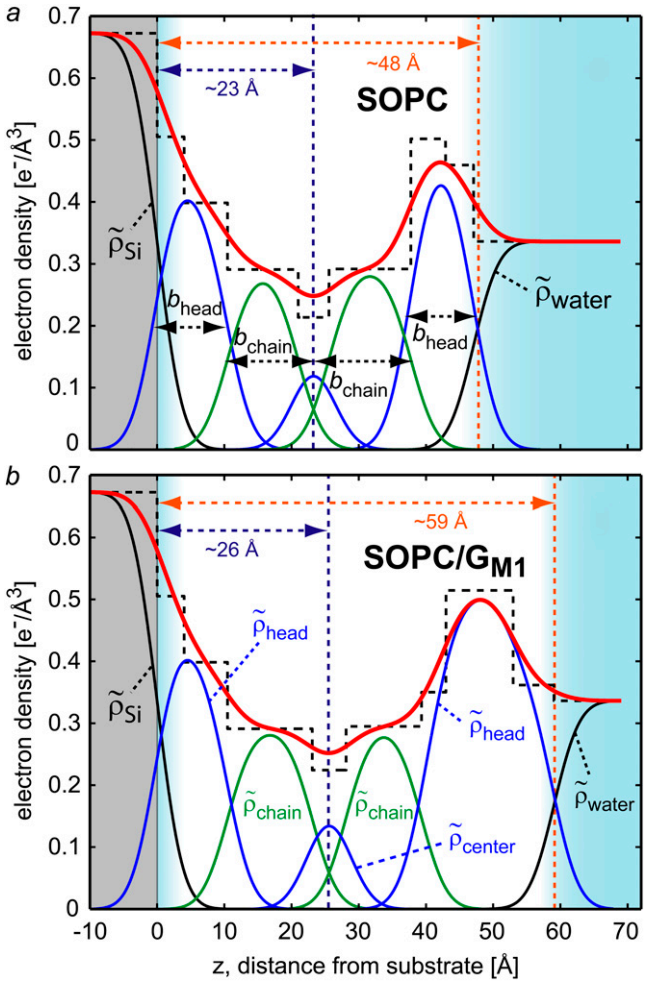

FIGURE 3 Electron density profiles (*red curves*) corresponding to the data in Fig. 2. (*a*) The SOPC bilayer appears highly symmetric with a thickness of 48 Å. (*b*) After incorporation of G_{M1}, the bilayer thickness is increased to 59 Å, predominantly due to a thickening of the distal leaflet. The profiles are decomposed to separately characterize the $\tilde{\rho}_{head}(z)$ electron density distributions of different bilayer regions, as described in Materials and Methods. The extracted thicknesses b_{head} and b_{chain} are indicated by arrows for each leaflet in panel *a*, and the electron densities $\tilde{\rho}_{chain}(z)$ (*green curves*), and $\tilde{\rho}_{center}(z)$ (*blue curves*) are indicated in panel *b*. The contributions from the substrate $\tilde{\rho}_{Si}(z)$ and the water $\tilde{\rho}_{water}(z)$ are also shown (*black curves*). The fitted slab models are represented as dotted lines.

The discrepancy between the raw data and the fitted curve at the lower q_z limit in Fig. 2 *b* is due to edge effects: in the limit of low q_z, the microfluidic chamber is illuminated along the full width by the x-ray beam and additional scattering from the glue at the chamber edge can be observed (see Data S1). The electron density profiles are presented as red curves in Fig. 3, *a* and *b*. The headgroup regions ($\tilde{\rho}_{head}(z)$), the acyl chains ($\tilde{\rho}_{chain}(z)$), and the region where the proximal and distal acyl chains meet ($\tilde{\rho}_{center}(z)$) are separately indicated. The extracted structural parameters with errors for $b_{chain/head}$ of ± 1 Å and for $\langle \rho_{chain/head} \rangle$ of ± 0.01 e$^-$/Å^3 are listed in Table 1.

It is well established that water can penetrate into the lipid headgroups (51), which may complicate an exact definition of bilayer thickness based on x-ray data. However, we estimate this value from the $\tilde{\rho}_{head}(z)$ distribution corresponding to the distal headgroup, where we define the half-maximum position at the outermost slope as bilayer thickness, as shown in Fig. 3. Using this analysis, the SOPC bilayer has an overall thickness of 48 Å and appears highly symmetric. The thicknesses of the proximal and distal leaflets (headgroups and acyl chains) are 23 Å and 25 Å, respectively, and b_{head} is 10 Å for both headgroups. Upon insertion of G_{M1}, however, the bilayer structure is significantly thickened (59 Å) and becomes asymmetric (Fig. 3 *b*). The thickening is marginal in the proximal leaflet (26 Å), whereas the distal leaflet thickness is 33 Å. This increase in thickness of the distal leaflet can be attributed to the headgroup region, where a significant increase in electron density is observed upon G_{M1} insertion.

By comparing the thicknesses of the distal leaflet before (25 ± 1 Å) and after (33 ± 1 Å) G_{M1} insertion, we find that the G_{M1} headgroup protrudes a distance of 8 ± 2 Å above the bilayer surface. Protrusion of the G_{M1} above the bilayer has been observed previously both with AFM (25) and x-ray diffraction (44), where it was shown that G_{M1} extends up to 12 Å above the surface of membranes in osmotically stretched stacked multibilayers. In the latter work, a full extension of the G_{M1} headgroup from the bilayer is reported, based on a comparison of the relative dimensions of G_{M1} and phosphatidylcholine headgroups. Assuming that G_{M1} headgroups in their fully extended conformation normal to the bilayer surface are 12 Å in height (44), our protrusion length of 8 ± 2 Å corresponds to an average headgroup tilt of $48 \pm 12°$ with respect to the bilayer normal.

TABLE 1 Parameters extracted from analysis of the x-ray reflectivity data

	b_{chain} (±1 Å)		$\langle\rho_{chain}\rangle$ (±0.01 e$^-$/Å^3)		b_{head} (±1 Å)		$\langle\rho_{head}\rangle$ (±0.01 e$^-$/Å^3)		SLB thickness (±1 Å)
	Proximal	Distal	Proximal	Distal	Proximal	Distal	Proximal	Distal	
SOPC	13	15	0.28	0.28	10	10	0.42	0.46	48
SOPC/G_{M1}	16	15	0.28	0.28	10	18	0.42	0.50	59
LD	14	14	0.28	0.28	11	15	0.43	0.44	54
LO	18	18	0.33	0.33	13	15	0.46	0.48	64
20 chol	17	16	0.33	0.33	12	13	0.42	0.43	58
20 chol + G_{M1}	16	16	0.33	0.33	12	17	0.42	0.43	61
30 chol	13	14	0.30	0.30	12	17	0.45	0.41	56
30 chol + G_{M1}	15	18	0.31	0.33	11	21	0.48	0.48	65
40 chol	14	14	0.29	0.29	12	16	0.46	0.40	56
40 chol + G_{M1}	14	17	0.30	0.33	11	22	0.48	0.49	64

The errors on the chain thickness b_{chain} and average chain electron density $\langle\rho_{chain}\rangle$ are estimated from the change in the corresponding slab parameters (ρ and d) necessary to increase the χ^2 of the fit by 20% or more. These errors are also assumed to apply to the headgroup parameters b_{head} and $\langle\rho_{head}\rangle$, since the precision of the $\tilde{\rho}_{head}(z)$-distributions is correlated to the precision of the acyl chains.

The similarity of the profiles for SOPC and SOPC/G_{M1} in the proximal leaflet (Fig. 3) shows that G_{M1} insertion only negligibly modifies the electron density of the proximal leaflet. This result suggests that G_{M1} inserts only into the distal leaflet of these supported membranes and does not flip into the bottom leaflet. By repeating our measurement of the reflectivity of the SOPC/G_{M1} membranes after three days, we verify that G_{M1} remains in the distal leaflet, as the reflectivity does not change over this timescale.

The electron density profiles further show that the headgroups are close to the substrate, and we do not observe the presence of a lubricating water layer separating the membrane from the substrate within our experimental resolution of 6 Å. Recent x-ray reflectivity experiments on single lipid bilayers report water layers of 4 Å (10) and 4.3 Å (11). However, a water layer of this size is difficult to define, considering the van der Waals diameter of a single water molecule of 2.75 Å (52), which is also similar to the typical length of a hydrogen bond. We suggest that there are individual water molecules bound to the polar lipid heads; however, we cannot isolate water molecules from the electron density of the headgroups.

We further investigate possible structural modifications in G_{M1} enriched lipid bilayers upon binding of cholera toxin. Cholera toxin can bind five G_{M1} receptors with its B subunit (CTB) and the resulting complex becomes the entry point for cholera toxin to enter the cell (8). Binding of a fluorescent conjugate of CTB (Alexa488 dye) to the membrane is evidenced by fluorescence microscopy, as the membrane surface after incubation with CTB shows bright homogeneous fluorescence (see Data S1). We verify with fluorescence microscopy that there is no nonspecific binding of CTB to SOPC bilayers lacking G_{M1} in a control experiment (data not shown). We find that the reflectivity of a SOPC/G_{M1} bilayer is not significantly changed and does not indicate the presence of an additional protein layer after incubation with CTB (Fig. 4). Thus, the formation of a CTB layer above the bilayer surface cannot be resolved with our reflectivity experiments. We also do not detect modification of the lipid bilayer structure upon CTB binding, in contrast to previous reports of lipid monolayer systems (26). In general, lipid bilayers are more stable than monolayers and can resist collapse upon binding of large molecules to the membrane surface (12). CTB lacks the large subunit A of cholera toxin and it has a relatively hollow ring structure which can be easily penetrated by water (53–55). Here, we suggest that a water-filled CTB layer on the membrane does not provide enough electron density contrast with respect to the excess water above the membrane.

Characterization of liquid-ordered and liquid-disordered SLBs

We next characterize the more complex system of lipid bilayers with multiple components capable of phase separation. Mixtures of cholesterol/DOPC/bSM can phase separate into fluid liquid-disordered (L_d) and condensed liquid-ordered

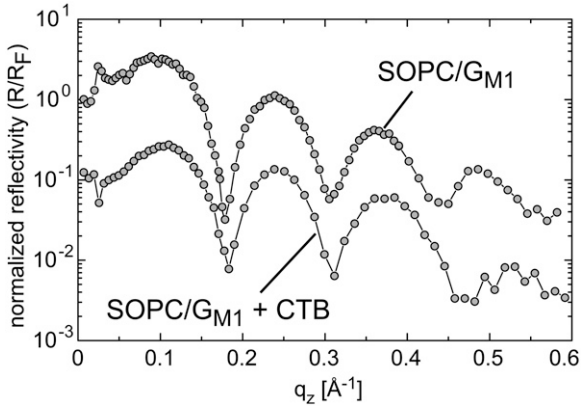

FIGURE 4 No measurable changes in the reflectivity of SOPC/G_{M1} SLBs before (*top*) and after (*bottom*) incubation with CTB. The lines connecting the data points are drawn for clarity of presentation and do not represent a fit to the data.

(L_o) phases, modeling lipid rafts in cell membranes (15). This phase separation is readily observed with fluorescence microscopy in fluid lipid bilayer vesicles (15,29). We choose two lipid compositions corresponding to pure L_d and pure L_o phases in the lipid phase diagram established for giant unilamellar vesicles (GUVs) of cholesterol, DOPC, and sphingomyelin (29). We estimate these mixtures based on a tie-line approximated from the similar GUV phase diagram of 1:1 DOPC/DPPC and 30 mol % cholesterol (30). According to our estimation, the fluid L_d phase has an approximate composition of 15:65:20 (cholesterol/DOPC/bSM) and the L_o phase has an approximate composition of 29:6:65 (cholesterol/DOPC/bSM).

To elucidate structural differences between the fluid L_d and the condensed L_o phase, we prepare separate SLBs with compositions of 15:65:19.5:0.5 (referred to as *LD*) and 29:6:64.5:0.5 (referred to as *LO*) mol % cholesterol/DOPC/bSM/TR-DPPE and measure them with reflectivity. The reflectivity data are shown in Fig. 5, the corresponding electron density profiles are plotted in Fig. 6, and the parameters extracted from fitting the data are summarized in Table 1. The electron density profile of *LD* shows similarities to the profile of a fluid SOPC bilayer (compare Fig. 3 *a* and Fig. 6 *a*). The acyl-chain thickness, b_{chain}, for both leaflets is 14 Å and the electron density $\langle\rho_{chain}\rangle$ is 0.28 $e^-/Å^3$. For the *LO* composition, the bilayer structure changes significantly. The *LO* bilayer is 10 Å thicker than the *LD* bilayer, as shown in Fig. 6 *b*. Our measured height difference is consistent with AFM experiments, where a relative height difference between L_o and L_d phases of 8 Å has been measured on SLBs of molar composition 0.67:1:1 (cholesterol/DOPC/SM) (16). For the *LO* bilayer, we measure a higher chain density $\langle\rho_{chain}\rangle$ of 0.33 $e^-/Å^3$ for both leaflets, as compared to 0.28 $e^-/Å^3$ for the *LD* bilayer. In both cases, the $\tilde{\rho}_{head}(z)$-distribution of the distal

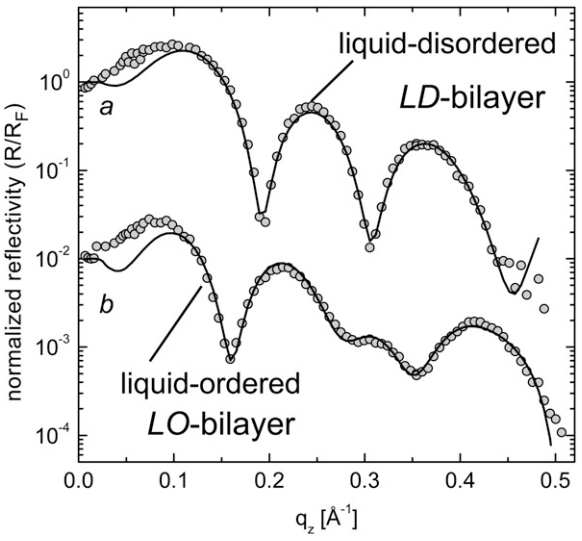

FIGURE 5 Normalized x-ray reflectivity of SLBs with compositions of 15:65:20 mol % (*LD*) and 29:6:65 mol % (*LO*) cholesterol/DOPC/bSM. Solid lines represent fits to the data.

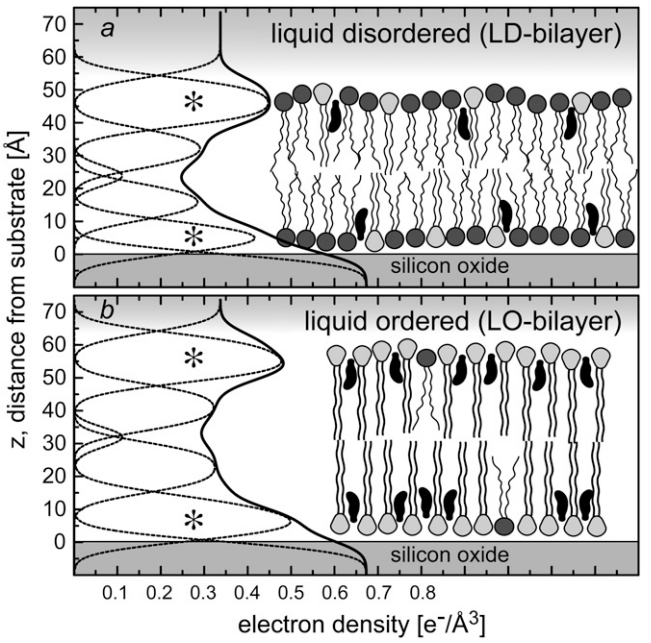

FIGURE 6 Electron density profiles of samples (*a*) *LD* and (*b*) *LO* (*solid lines*). The individual contributions to the profile, $\tilde{\rho}_{chain}(z)$, $\tilde{\rho}_{head}(z)$, and $\tilde{\rho}_{center}(z)$, are plotted as shaded dotted lines. The headgroup electron densities $\tilde{\rho}_{head}(z)$ are additionally marked with an asterisk (*). Sketches represent the molar compositions of cholesterol (*solid*), DOPC (*dark shaded*), and bSM (*light shaded*) in the *LD* and *LO* bilayers and illustrate the differences in bilayer condensation and thickness.

headgroups is broadened compared to the $\tilde{\rho}_{head}(z)$-distribution of the proximal headgroups, indicating that the membrane surface facing the water is not as uniform as the opposite surface facing the substrate. The variety of lipid constituents with different chain length in natural brain sphingomyelin may additionally contribute to this broadening of the headgroups.

Combining these results, we can quantitatively describe the differences between liquid-ordered and liquid-disordered lipid bilayers in terms of the electron density and thickness of the acyl chains. Here, both an electron density $\langle\rho_{chain}\rangle$ of 0.28 ± 0.01 $e^-/Å^3$ and chain thickness b_{chain} of 14 ± 1 Å are characteristic of the *LD*, fluid-disordered bilayer leaflets, whereas an electron density $\langle\rho_{chain}\rangle$ of 0.33 ± 0.01 $e^-/Å^3$ and chain thickness b_{chain} of 17 ± 1 Å is representative of the *LO*, condensed bilayer leaflets. The structural differences between these two phases are reflected in the corresponding sketches of the bilayer structure in Fig. 6, showing the *LO* bilayer as thickened with stretched and packed acyl chains as compared to the *LD* bilayer.

Model lipid raft SLBs and the asymmetric insertion of G_{M1}

After separately characterizing *LD* and *LO* bilayers, we now investigate SLBs with an equimolar lipid ratio of DOPC and bSM and varying amount of cholesterol. Three SLBs of

cholesterol/DOPC/bSM/TR-DPPE with molar percentages 20:40:39.5:0.5 (referred to as 20 chol), 30:35:34.5:0.5 (30 chol), and 40:30:29.5:0.5 (40 chol) are measured at room temperature. Within the GUV phase diagram at room temperature, 20 chol is clearly in the L_o/L_d coexistence region, while 30 chol is located at the onset of L_o/L_d coexistence, and 40 chol is in the single phase region (32). The reflectivities of these SLBs are presented in Fig. 7 *a* and the corresponding profiles are presented in Fig. 8. Extracted parameters are listed in Table 1. In mixture 20 chol, we observe a high chain electron density $\langle\rho_{chain}\rangle$ of 0.33 $e^-/Å^3$ in both leaflets and a bilayer thickness of 58 Å. By contrast, mixtures 30 chol and 40 chol show lower electron densities of the chain regions (0.30 and 0.29 $e^-/Å^3$, respectively), and both have a thickness of 56 Å. Comparing these samples to the *LD* and *LO* reference samples, 20 chol shows strong structural similarity to the *LO* bilayer, while the chain densities and bilayer thicknesses of samples 30 chol and 40 chol are similar to the fluid *LD* bilayer. We then use our protocol for asymmetric G_{M1} incorporation into SLBs to assess the structural effect of G_{M1} on the samples 20 chol, 30 chol, and 40 chol. After G_{M1} insertion, these samples are subsequently referred to as 20 chol + G_{M1}, 30 chol + G_{M1}, and 40 chol + G_{M1}. The reflectivity data are presented in Fig. 7 *b* and the electron density profiles are plotted in Fig. 8. The electron density profile of 20 chol + G_{M1} shows only minimal changes compared to 20 chol; namely, a slight increase in bilayer thickness of 3 Å due to a broader distal headgroup. The electron density profiles of samples 30 chol + G_{M1} and 40 chol + G_{M1} show a thickening of the SLBs of 9 and 8 Å, respectively, and a strong increase of $\langle\rho_{head}\rangle$ in the distal headgroup region from 0.41 to 0.48 $e^-/Å^3$ and from 0.40 to 0.49 $e^-/Å^3$, respectively. Looking only at the acyl-chain region of the distal leaflet, there is an increase in thickness from 14 to 18 Å for 30 chol + G_{M1} and from 14 to 17 Å for 40 chol + G_{M1}. In this region, there is also an increase in electron density from 0.30 to 0.33 $e^-/Å^3$ for 30 chol + G_{M1} and from 0.29 to 0.33 $e^-/Å^3$ for 40 chol + G_{M1}. The proximal acyl chains remain relatively unaffected, although the electron density slightly increases from 0.30 to 0.31 $e^-/Å^3$ for 30 chol + G_{M1} and from 0.29 to 0.30 $e^-/Å^3$ for 40 chol + G_{M1}.

Although we cannot quantify the amount of G_{M1} inserted into the SLBs, or compare G_{M1} affinity among different compositions, our results indicate that all three investigated lipid mixtures containing cholesterol, DOPC, and bSM undergo structural modifications upon G_{M1} insertion. The most prominent effect of G_{M1} is observed for the 30 chol + G_{M1} and 40 chol + G_{M1} samples: the distal leaflets of 30 chol + G_{M1} and 40 chol + G_{M1} have a structure similar to the leaflets of the *LO* bilayer, while the proximal leaflets maintain structural similarity to the *LD* bilayer. These results suggest that G_{M1} can modify acyl-chain packing in leaflets containing cholesterol differently than in leaflets lacking cholesterol, such as SOPC. We do not expect the incorporation of ovine G_{M1} to increase the total fraction of saturated acyl chains in the mixture. Thus, we attribute our observed increase in acyl chain density and the shift in structural similarity from *LD* to *LO* to interaction of G_{M1} with cholesterol and sphingomyelin. G_{M1} can moderate lipid packing in cholesterol enriched lipid mixtures (56,57); and there may be an attractive electrostatic interaction between the sialic acid of G_{M1} and the positively-charged choline headgroups of DOPC and bSM.

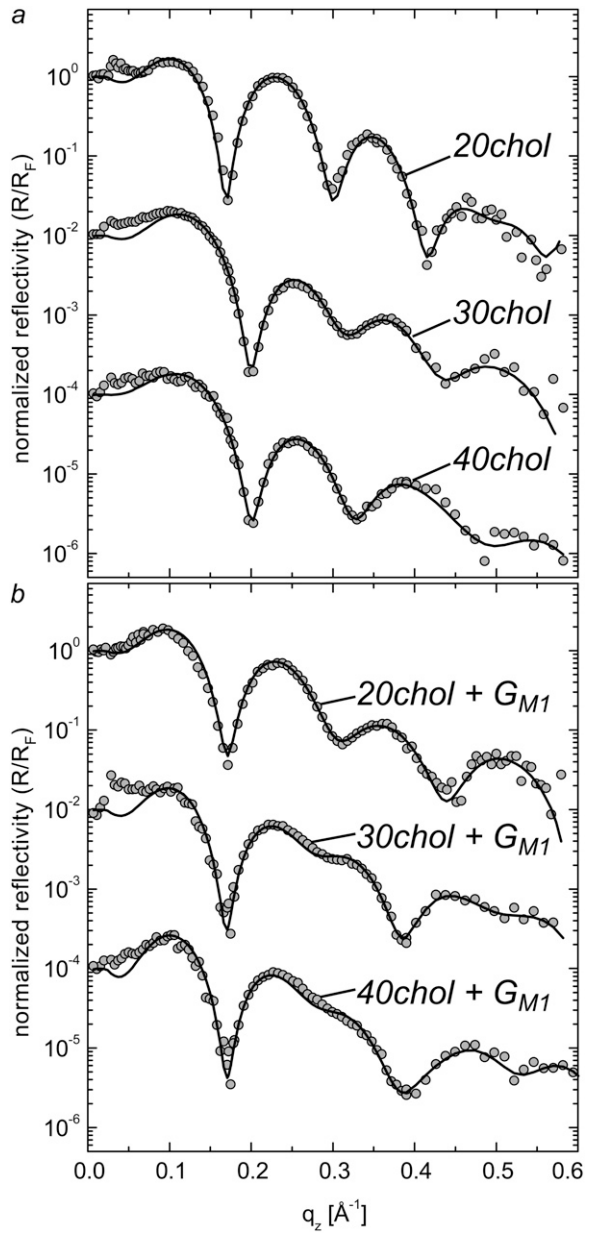

FIGURE 7 Normalized reflectivity of cholesterol/DOPC/bSM SLBs with equimolar composition of DOPC and bSM, before (*a*) and after (*b*) G_{M1} incorporation. Solid lines represent fits to the data.

Lipid diffusion and fluorescence microscopy

In addition to x-ray reflectivity, we image the SLBs with fluorescence microscopy to characterize microscopic features

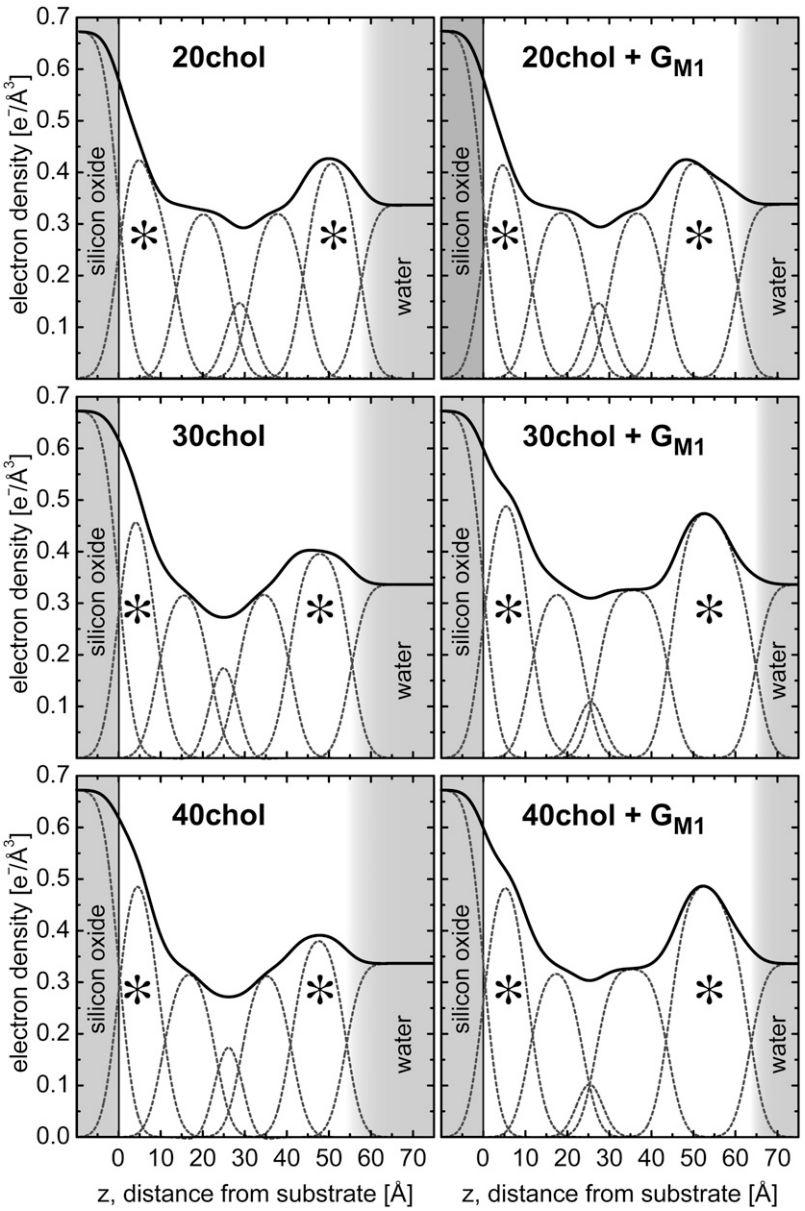

FIGURE 8 Electron density profiles of cholesterol/DOPC/bSM SLBs with equimolar composition of DOPC and bSM, before and after G_{M1} incorporation (*solid lines*). The detailed electron density contributions to the profile are plotted as shaded dotted lines. The headgroup electron densities are marked with an asterisk (*).

in the membranes and to measure the lateral lipid diffusion in the bilayers. The compact sample chambers that we use allow for fluorescence microscopy imaging on the same SLBs measured with x-ray reflectivity (27). Before incubation with G_{M1}, all of the SLBs have homogeneous fluorescence and we do not observe microscopic phase separation in the samples 20 chol, 30 chol, and 40 chol. An example fluorescence micrograph of 20 chol is shown in Fig. 9 *a*. Although this lipid mixture is known to separate into microscopic L_o and L_d phases at room temperature in GUVs, as visualized by partitioning of the dye into the L_d phase (32), our sample shows a uniform fluorescence. Whereas L_o/L_d coexistence in SLBs with submicron domains are reported by AFM studies on mica (16,17,58), surfaces with defined topography (59), and glass slides (60), we do not observe microscopic phases on the SiO_2 substrates (surface roughness 3 Å) that we use for reflectivity. It is possible that our model lipid raft mixtures have nanoscopic domains that do not grow to microscopic dimensions in the vicinity of the solid interfaces (19,58).

However, we do observe microscopic features upon incorporation of G_{M1} into the samples 20 chol + G_{M1}, 30 chol + G_{M1}, and 40 chol + G_{M1}. Solid spots ~ 3 μm in diameter appear which exclude TR-DPPE that are not present before G_{M1} incubation. Fig. 9 *b* shows a micrograph of sample 20 chol + G_{M1}. The solid spots are also observed on the samples 30 chol + G_{M1} and 40 chol + G_{M1} (see Data S1). In sample 20 chol + G_{M1}, we see shaded spots (~3 μm) on the membrane surface in coexistence with the dark spots (Fig. 9 *b*). To elucidate whether the spots are lipid domains or surface defects, we examine the temperature behavior of the

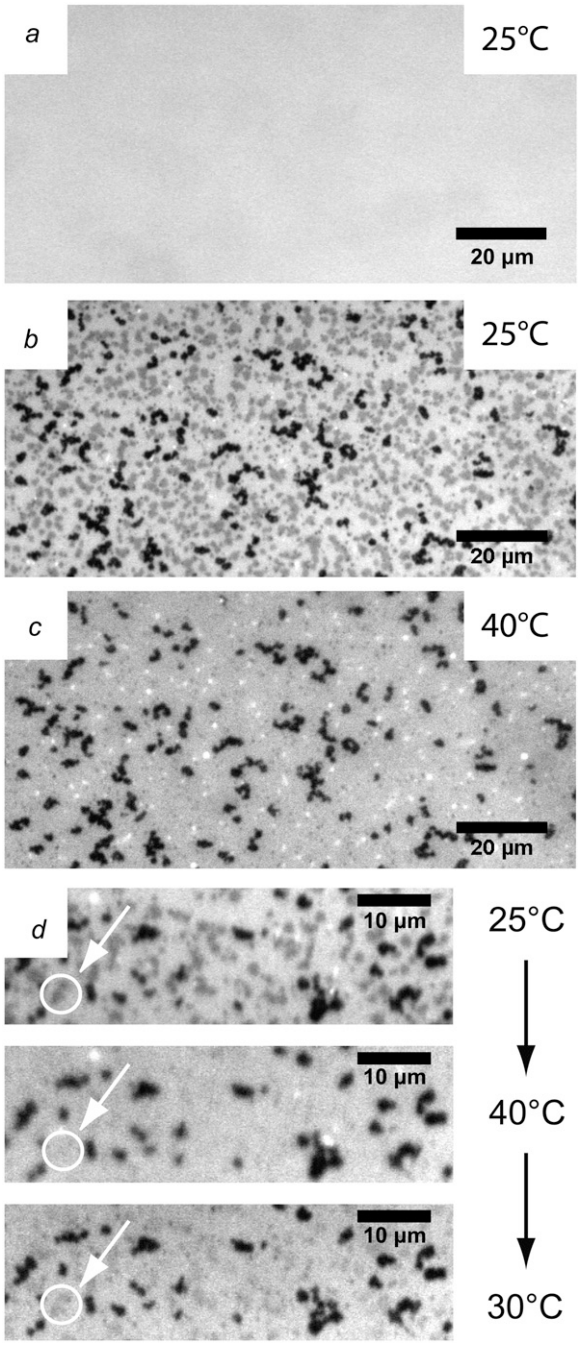

FIGURE 9 Fluorescence micrographs of cholesterol/DOPC/bSM SLBs. (*a*) Before G_{M1} addition, sample 20 chol shows uniform fluorescence. (*b*) Solid spots appear after 4 h incubation with excess G_{M1}. Sample 20 chol + G_{M1} shows shaded and solid domains at room temperature (25°C). (*c*) Upon increasing the temperature to 40°C, the shaded domains vanish and the solid domains remain unchanged. (*d*) Closeup micrographs: The open circle is a guide to the eye and highlights a pinned shaded domain. The temperature cycle (25°C → 40°C → 30°C) shows the shaded domains reappearing at their former positions upon recooling.

SLBs. The dark spots persist upon heating and do not change in shape or size up to a temperature of 70°C. Qualitative reference to the GUV phase diagram show that our lipid mixtures do not exhibit lipid phase coexistence at >50°C (32). Thus, the stability of the solid spots, combined with their strong exclusion of the dye, suggest that they are membrane defects such as pinned lipid or receptor aggregates or bare surface areas. Previous experiments show that membrane rupture and hole formation can be induced by increasing the tension in the membrane (33); attractive interactions of G_{M1} with adjacent lipids could also promote the local packing of lipids, resulting in the formation of pinholes in the membrane. Interestingly, the shaded spots in sample 20 chol + G_{M1} disappear upon heating to 40°C and reappear upon cooling in the same positions (Fig. 9, *c* and *d*). The shaded spots thus may be lateral lipid domains that exclude the fluorescent dye. Previous studies have demonstrated that lipid domains in SLBs lack the reversible phase behavior characteristic of fluid membranes and the domains can be pinned to the substrate (19,61). The size of the shaded spots is comparable to the size of the L_o phases recently reported by AFM measurements on SLBs of molar composition 0.67:1:1 (cholesterol/DOPC/bSM) (16), suggesting that microscopic L_o phases can form in the presence of the silicon oxide interface upon G_{M1} insertion. In the same work, two-focus scanning fluorescence correlation spectroscopy is used to separately determine the diffusion constants for the L_d phase ($3.5 \pm 0.3\ \mu m^2/s$) and for the L_o phase ($0.1 \pm 0.02\ \mu m^2/s$).

To assess whether G_{M1} modifies the fluidity of the bilayer, we measure the lateral diffusion coefficients of TR-DPPE in the samples 20 chol, 30 chol, and 40 chol, before and after insertion of G_{M1} using continuous bleaching. The continuous bleaching method allows diffusion constants to be measured with a standard fluorescent microscopy setup and does not require laser bleaching (22). The diffusion coefficients we determine with continuous bleaching represent the laterally averaged lipid diffusion in a circular spot 180-μm diameter and it is therefore not possible to distinguish between separate diffusion coefficients in coexisting phases. We measure diffusion coefficients for samples 20 chol, 30 chol, and 40 chol of (0.45 ± 0.03, 0.22 ± 0.01, and 0.12 ± 0.01) $\mu m^2/s$, respectively. The error is estimated as experimental standard deviation. Our diffusion data shows the general trend that diffusion is reduced as the concentration of cholesterol is increased. After these samples are incubated with excess G_{M1}, we measure diffusion constants of (0.10 ± 0.02, 0.09 ± 0.01, and 0.03 ± 0.01) $\mu m^2/s$ for samples 20 chol + G_{M1}, 30 chol + G_{M1}, and 40 chol + G_{M1}, respectively. Thus, the addition of G_{M1} to the bilayer reduces the lipid fluidity by >50%.

CONCLUSION

Using x-ray reflectivity, we study the detailed electron density profiles of a series of single SLBs with few-Ångström resolution. The structural differences between fluid *LD* and

SOPC bilayers, and liquid-ordered *LO* bilayers are characterized in terms of leaflet dimensions, acyl and headgroup electron densities, and bilayer thicknesses. We resolve asymmetric structural changes across lipid bilayer leaflets induced by the incorporation of the membrane receptor G_{M1} into the outer leaflet. SOPC bilayers become asymmetric with the addition of G_{M1}, and the proximal headgroups become 8 Å thicker. The structural changes to the bilayer induced by G_{M1} are different among the cholesterol/bSM/DOPC bilayers. In samples 30 chol + G_{M1} and 40 chol + G_{M1}, G_{M1} both increases the acyl-chain density of the outer leaflet by 10–14%, and reduces the lipid diffusion constant by 50%. These changes shift the structural similarity of the outer lipid leaflets of these samples from *LD* to *LO*. Upon G_{M1} incorporation, sample 20 chol + G_{M1} retains a structure similar to the *LO* bilayer and the acyl-chain electron densities are unaffected, but the distal headgroups become 4 Å thicker and lipid diffusion is reduced by >50%. The fluorescence micrographs and diffusion measurements indicate how G_{M1} incorporation generally slows lipid diffusion and induces lateral microscopic domains in the cholesterol/bSM/DOPC bilayers. Our observations suggest that receptor molecules can induce complex structural changes to the lipid bilayer that depend upon lipid composition and fluidity.

In conclusion, x-ray reflectivity in combination with fluorescence microscopy is well suited for characterizing the structural details of model lipid bilayers, and can aid in understanding how membrane receptors affect the internal structure of cell membranes. Further x-ray reflectivity studies of biologically active molecules that intercalate lipid bilayers, including proteins and receptors, may elucidate how external molecules interact with different regions of the lipid bilayer and control the organization of the membrane.

SUPPLEMENTARY MATERIAL

To view all of the supplemental files associated with this article, visit www.biophysj.org.

We acknowledge the European Synchrotron Radiation Facility for provision of synchrotron radiation facilities and we thank Till H. Metzger for assistance in using the beamline ID01 and Harald Müller for assistance in the chemistry laboratory. We are grateful to Martin Huth for help with the synchrotron measurements.

We thank the Alexander von Humboldt Foundation and the MIT-Germany Program for travel funds. Financial support by the Nanosystems Initiative Munich (NIM) is gratefully acknowledged. This work was funded in part through the Robert T. Haslam Chair at the Massachusetts Institute of Technology and the German Federal Ministry of Education and Research (BMBF grant No. 03RA6LMU).

REFERENCES

1. Janmey, P. A., and P. K. J. Kinnunen. 2006. Biophysical properties of lipids and dynamic membranes. *Trends Cell Biol.* 16:538–546.
2. Simons, K., and E. Ikonen. 1997. Functional rafts in cell membranes. *Nature*. 387:569–572.
3. Brown, D. A., and E. London. 2000. Structure and function of sphingolipid- and cholesterol-rich membrane rafts. *J. Biol. Chem.* 275: 17221–17224.
4. Anderson, R. G. W., and K. Jacobson. 2002. A role for lipid shells in targeting proteins to caveolae, rafts, and other lipid domains. *Science*. 296:1821–1825.
5. Simons, K., and E. Ikonen. 2000. How cells handle cholesterol. *Science*. 290:1721–1726.
6. Maxfield, F. R., and I. Tabas. 2005. Role of cholesterol and lipid organization in disease. *Nature*. 438:612–621.
7. Sprong, H., P. van der Sluijs, and G. van Meer. 2001. How proteins move lipids and lipids move proteins. *Nat. Rev. Mol. Cell Biol.* 2:504–513.
8. Lencer, W. I., T. R. Hirst, and R. K. Holmes. 1999. Membrane traffic and the cellular uptake of cholera toxin. *Biochim. Biophys. Acta*. 1450: 177–190.
9. Richter, R. P., and A. Brisson. 2003. Characterization of lipid bilayers and protein assemblies supported on rough surfaces by atomic force microscopy. *Langmuir*. 19:1632–1640.
10. Miller, C. E., J. Majewski, T. Gog, and T. L. Kuhl. 2005. Characterization of biological thin films at the solid-liquid interface by x-ray reflectivity. *Phys. Rev. Lett.* 94:238104.
11. Nováková, E., K. Giewekemeyer, and T. Salditt. 2006. Structure of two-component lipid membranes on solid support: an x-ray reflectivity study. *Phys. Rev. E Stat. Nonlin. Soft Matter Phys.* 74:051911.
12. Horton, M. R., C. Reich, A. P. Gast, J. O. Rädler, and B. Nickel. 2007. Structure and dynamics of crystalline protein layers bound to supported lipid bilayers. *Langmuir*. 23:6263–6269.
13. Krueger, S. 2001. Neutron reflection from interfaces with biological and biomimetic materials. *Curr. Opin. Colloid Interface Sci.* 6:111–117.
14. Crane, J. M., V. Kiessling, and L. K. Tamm. 2005. Measuring lipid asymmetry in planar supported bilayers by fluorescence interference contrast microscopy. *Langmuir*. 21:1377–1388.
15. Dietrich, C., L. A. Bagatolli, Z. N. Volovyk, N. L. Thompson, M. Levi, K. Jacobson, and E. Gratton. 2001. Lipid rafts reconstituted in model membranes. *Biophys. J.* 80:1417–1428.
16. Chiantia, S., J. Ries, N. Kahya, and P. Schwille. 2006. Combined AFM and two-focus SFCS study of raft-exhibiting model membranes. *ChemPhysChem*. 7:2409–2418.
17. Yuan, C., J. Furlong, P. Burgos, and L. J. Johnston. 2002. The size of lipid rafts: an atomic force microscopy study of ganglioside GM1 domains in sphingomyelin/DOPC/cholesterol membranes. *Biophys. J.* 82:2526–2535.
18. Samsonov, A. V., I. Mihalyov, and F. S. Cohen. 2001. Characterization of cholesterol-sphingomyelin domains and their dynamics in bilayer membranes. *Biophys. J.* 81:1486–1500.
19. Garg, S., J. Ruhe, K. Ludtke, R. Jordan, and C. A. Naumann. 2007. Domain registration in raft-mimicking lipid mixtures studied using polymer-tethered lipid bilayers. *Biophys. J.* 92:1263–1270.
20. Bagatolli, L. A. 2006. To see or not to see: lateral organization of biological membranes and fluorescence microscopy. *Biochim. Biophys. Acta*. 1758:1541–1556.
21. Axelrod, D., D. E. Koppel, J. Schlessinger, E. Elson, and W. W. Webb. 1976. Mobility measurement by analysis of fluorescence photobleaching recovery kinetics. *Biophys. J.* 16:1055–1069.
22. Dietrich, C., R. Merkel, and R. Tampé. 1997. Diffusion measurement of fluorescence-labeled amphiphilic molecules with a standard fluorescence microscope. *Biophys. J.* 72:1701–1710.
23. Weng, K. C., J. L. Kanter, W. H. Robinson, and C. W. Frank. 2006. Fluid supported lipid bilayers containing monosialoganglioside GM1: a QCM-D and FRAP study. *Colloids Surf. B Biointerfaces*. 50: 76–84.

24. Yamazaki, V., O. Sirenko, R. J. Schafer, and J. T. Groves. 2005. Lipid mobility and molecular binding in fluid lipid membranes. *J. Am. Chem. Soc.* 127:2826–2827.
25. Yuan, C., and L. J. Johnston. 2001. Atomic force microscopy studies of ganglioside GM1 domains in phosphatidylcholine and phosphatidylcholine/cholesterol bilayers. *Biophys. J.* 81:1059–1069.
26. Miller, C. E., J. Majewski, R. Faller, S. Satija, and T. L. Kuhl. 2004. Cholera toxin assault on lipid monolayers containing ganglioside G_{M1}. *Biophys. J.* 86:3700–3708.
27. Reich, C., M. B. Hochrein, B. Krause, and B. Nickel. 2005. A microfluidic setup for studies of solid-liquid interfaces using x-ray reflectivity and fluorescence microscopy. *Rev. Sci. Instrum.* 76:095103.
28. Hochrein, M. B., C. Reich, B. Krause, J. O. Rädler, and B. Nickel. 2006. Structure and mobility of lipid membranes on a thermoplastic substrate. *Langmuir.* 22:538–545.
29. Veatch, S. L., and S. L. Keller. 2005. Miscibility phase diagrams of giant vesicles containing sphingomyelin. *Phys. Rev. Lett.* 94:148101.
30. Veatch, S. L., I. V. Polozov, K. Gawrisch, and S. L. Keller. 2004. Liquid domains in vesicles investigated by NMR and fluorescence microscopy. *Biophys. J.* 86:2910–2922.
31. MacDonald, R. C., R. I. MacDonald, B. P. M. Menco, K. Takeshita, N. K. Subbarao, and L. Hu. 1991. Small-volume extrusion apparatus for preparation of large, unilamellar vesicles. *Biochim. Biophys. Acta.* 1061:297–303.
32. Horton, M. R., J. O. Rädler, and A. P. Gast. 2006. Phase behavior and the partitioning of caveolin-1 scaffolding domain peptides in model lipid bilayers. *J. Colloid Interface Sci.* 304:67–76.
33. Tamm, L. K., and H. M. McConnell. 1985. Supported phospholipid bilayers. *Biophys. J.* 47:105–113.
34. Cantú, L., M. Corti, E. Del Favero, E. Muller, A. Raudino, and S. Sonnino. 1999. Thermal hysteresis in ganglioside micelles investigated by differential scanning calorimetry and light-scattering. *Langmuir.* 15: 4975–4980.
35. Basu, A., and R. H. Glew. 1985. Characterization of the activation of rat liver β-glucosidase by sialosylgangliotetraosylceramide. *J. Biol. Chem.* 260:13067–13073.
36. Bach, D., I. R. Miller, and B.-A. Sela. 1982. Calorimetric studies on various gangliosides and ganglioside-lipid interactions. *Biochim. Biophys. Acta.* 686:233–239.
37. Spiegel, S., J. Schlessinger, and P. H. Fishman. 1984. Incorporation of fluorescent gangliosides into human fibroblasts: mobility, fate, and interaction with fibronectin. *J. Cell Biol.* 99:699–704.
38. Wang, R., J. Shi, A. N. Parikh, A. P. Shreve, L. Chen, and B. I. Swanson. 2004. Evidence for cholera aggregation on GM_1-decorated lipid bilayers. *Colloids Surf. B Biointerfaces.* 33:45–51.
39. Israelachvili, J. N., D. J. Mitchell, and B. W. Ninham. 1977. Theory of self-assembly of lipid bilayers and vesicles. *Biochim. Biophys. Acta.* 470:185–201.
40. Majewski, J., T. L. Kuhl, K. Kjaer, and G. S. Smith. 2001. Packing of ganglioside-phospholipid monolayers: an x-ray diffraction and reflectivity study. *Biophys. J.* 81:2707–2715.
41. Small, D. M. 1967. Phase equilibria and structure of dry and hydrated egg lecithin. *J. Lipid Res.* 8:551–557.
42. Liu, Y., and J. F. Nagle. 2004. Diffuse scattering provides material parameters and electron density profiles of biomembranes. *Phys. Rev. E Stat. Nonlin. Soft Matter Phys.* 69:040901.
43. Petrache, H. I., S. E. Feller, and J. F. Nagle. 1997. Determination of component volumes of lipid bilayers from simulations. *Biophys. J.* 72: 2237–2242.
44. McIntosh, T. J., and S. A. Simon. 1994. Long- and short-range interactions between phospholipid/ganglioside G_{M1} bilayers. *Biochemistry.* 33:10477–10486.
45. Parratt, L. G. 1954. Surface studies of solids by total reflection of x-rays. *Phys. Rev.* 95:359.
46. Pershan, P. S. 1994. X-ray or neutron reflectivity: limitations in the determination of interfacial profiles. *Phys. Rev. E Stat. Phys. Plasmas Fluids Relat. Interdiscip. Topics.* 50:2369–2372.
47. Névot, L., and P. Croce. 1980. Characterization of surfaces by grazing x-ray reflection—application to study of polishing of some silicate-glasses. *Rev. Phys. Appl.* 15:761–779.
48. de Boer, D. K. G. 1994. Influence of the roughness profile on the specular reflectivity of x-rays and neutrons. *Phys. Rev. B.* 49:5817–5820.
49. Lambacher, A., and P. Fromherz. 1996. Fluorescence interference-contrast microscopy on oxidized silicon using a monomolecular dye layer. *Appl. Phys. A.* 63:207–216.
50. Reference deleted in proof.
51. Wiener, M. C., G. I. King, and S. H. White. 1991. Structure of a fluid dioleoylphosphatidylcholine bilayer determined by joint refinement of x-ray and neutron diffraction data. I. Scaling of neutron data and the distributions of double bonds and water. *Biophys. J.* 60:568–576.
52. Zhang, Y., and Z. Xu. 1995. Atomic radii of noble gas elements in condensed phases. *Am. Mineral.* 80:670–675.
53. Zhang, R., M. L. Westbrook, E. M. Westbrook, D. L. Scott, Z. Otwinowski, P. R. Maulik, R. A. Reed, and G. G. Shipley. 1995. The 2.4 Å crystal structure of cholera toxin B subunit pentamer: choleragenoid. *J. Mol. Biol.* 251:550–562.
54. Merritt, E. A., S. Sarfaty, F. V. D. Akker, C. L'Hoir, J. A. Martial, and W. G. Hol. 1994. Crystal structure of cholera toxin B-pentamer bound to receptor G_{M1} pentasaccharide. *Protein Sci.* 3:166–175.
55. Ribi, H. O., D. S. Ludwig, K. L. Mercer, G. K. Schoolnik, and R. D. Kornberg. 1988. Three-dimensional structure of cholera toxin penetrating a lipid membrane. *Science.* 239:1272–1276.
56. Hammond, A. T., F. A. Heberle, T. Baumgart, D. Holowka, B. Baird, and G. W. Feigenson. 2005. Crosslinking a lipid raft component triggers liquid ordered-liquid disordered phase separation in model plasma membranes. *Proc. Natl. Acad. Sci. USA.* 102:6320–6325.
57. Dietrich, C., Z. N. Volovyk, M. Levi, N. L. Thompson, and K. Jacobson. 2001. Partitioning of Thy-1, G_{M1}, and cross-linked phospholipid analogs into lipid rafts reconstituted in supported model membrane monolayers. *Proc. Natl. Acad. Sci. USA.* 98:10642–10647.
58. Jensen, M., E. Morris, and A. Simonsen. 2007. Domain shapes, coarsening, and random patterns in ternary membranes. *Langmuir.* 23:8135–8141.
59. Yoon, T.-Y., C. Jeong, S.-W. Lee, J. H. Kim, M. C. Choi, S.-J. Kim, M. W. Kim, and S.-D. Lee. 2006. Topographic control of lipid-raft reconstitution in model membranes. *Nat. Mater.* 5:281–285.
60. Seu, K. J., A. P. Pandey, F. Haque, E. A. Proctor, A. E. Ribbe, and J. S. Hovis. 2007. Effect of surface treatment on diffusion and domain formation in supported lipid bilayers. *Biophys. J.* 92:2445–2450.
61. Stottrup, B. L., S. L. Veatch, and S. L. Keller. 2004. Nonequilibrium behavior in supported lipid membranes containing cholesterol. *Biophys. J.* 86:2942–2950.